

Anomalous Hall effect emerging from field-induced Weyl nodes in SmAlSi

Yuxiang Gao,^{1,2} Shiming Lei,^{1,2,*} Eleanor M. Clements,^{3,4} Yichen Zhang,^{1,2} Xue-Jian Gao,⁵
Songxue Chi,⁶ Kam Tuen Law,⁵ Ming Yi,^{1,2} Jeffrey W. Lynn,³ and Emilia Morosan^{1,2,†}

¹*Department of Physics and Astronomy, Rice University, Houston, Texas 77005, USA*

²*Rice Center for Quantum Materials, Rice University, Houston, Texas 77005, USA*

³*NIST Center for Neutron Research, National Institute of Standards and Technology, Gaithersburg, Maryland 20899, USA*

⁴*Materials Science and Technology Division, Oak Ridge National Laboratory, Oak Ridge, Tennessee 37831, USA*

⁵*Department of Physics, Hong Kong University of Science and Technology, Clear Water Bay, Hong Kong, China*

⁶*Neutron Scattering Division, Oak Ridge National Laboratory, Oak Ridge, Tennessee 37831, USA*

(Dated: August 27, 2024)

The intrinsic anomalous Hall effect (AHE) has been reported in numerous ferromagnetic (FM) Weyl semimetals. However, AHE in the antiferromagnetic (AFM) or paramagnetic (PM) state of Weyl semimetals has been rarely observed experimentally. Different mechanisms have been proposed to account for the emergence of AHE from different types of magnetic order. In this paper, we propose a new model that explains the observed AHE in both the AFM and PM states of non-centrosymmetric Weyl semimetal SmAlSi. The newly-proposed mechanism is based on magnetic field-induced Weyl nodes evolution, which qualitatively explains the temperature dependence of the anomalous Hall conductivity (AHC), which displays unconventional power law behavior in both the AFM and PM states of SmAlSi.

Magnetic Weyl semimetals have garnered a lot of interest in recent years because of the interplay between electronic correlations and topology [1–6]. Magnetism drastically increases the number of possible symmetries, from 230 crystalline space groups to 1651 magnetic space groups if we only consider the commensurate order, allowing for the tunability of topology through the magnetic structure. In magnetic Weyl semimetals, Weyl fermions can mediate magnetic order through nesting between different Weyl pockets [6–10]. Furthermore, the Weyl nodes of different chirality in magnetic Weyl semimetals bring about a broad range of magnetotransport and spectroscopic properties [11–16]. Among these, the anomalous Hall effect (AHE) in Weyl semimetals stands out, especially in contrast to the AHE in normal ferromagnets, *e.g.*, iron [17–21]. In the latter, the spin-orbit interaction and the net magnetization M are essential to establishing a non-zero AHE, where the anomalous Hall conductivity (AHC) is found to be proportional to M in FM materials [22]. By contrast, the Weyl nodes behave as effective magnetic monopoles, generating strong Berry curvature which, in turn, acts like an effective magnetic field in momentum space. In this scenario, the FM order is no longer required for a Weyl semimetal to host non-zero AHE [23–25].

To date, AHE has been reported in a few magnetic Weyl semimetals [28–36], associated with different mechanisms. The AHE shows linear dependence on the magnetization M in some FM compounds (Fe_3Sn_2 , MnSi , PrAlGe , Mn_5Ge_3 , $\text{Co}_3\text{Sn}_2\text{S}_2$ and Fe_3GeTe_2) [28, 32–36], but not in AFM and non-magnetic (NM) materials (ZrTe_5 , $(\text{Nd}, \text{Gd})\text{PtBi}$, $\text{Mn}_3(\text{Ge}, \text{Sn})$ and KV_3Sb_5)

[23, 29–31, 37]. These AFM or NM Weyl semimetals do not host Weyl nodes without further breaking the time-reversal symmetry. Different AHE mechanisms have recently been proposed to explain the AHE in the absence of FM order [1, 39, 40]. Though supported theoretically, the AHE has not been found in materials that host Weyl nodes without time-reversal symmetry breaking. This precludes further development of a theoretical understanding of the AHE mechanisms in these materials.

Here, we report large AHE in the AFM and PM state of SmAlSi, which is a member of the non-centrosymmetric class of compounds $R\text{Al}(\text{Si}, \text{Ge})$ ($R = \text{La}, \text{Ce}, \text{Pr}, \text{Nd}, \text{Sm}$) [4, 6, 13, 26, 38, 41–43]. Moreover, we propose a new mechanism to account for the AHE in non-FM materials without a center of symmetry. This mechanism is based on the displacement of the Weyl nodes to points with different momenta upon the application of a magnetic field, which results in regions with non-zero Chern numbers in the first Brillouin zone. The Weyl points and Kramers nodal lines (KNLs) in the PM state of SmAlSi have been investigated through density functional theory (DFT) calculations, angle-resolved photoemission spectroscopy (ARPES) and angle-dependent quantum oscillation (QO) measurements [27]. In addition to the previous report of the topological Hall effect (THE) in the intermediate-field A phase [26], here we report large AHE in the AFM ground state *and* in the PM state of SmAlSi up to 100 K. This is distinct from the AHE in CeAlSi, CeAlGe, PrAlSi and PrAlGe [4, 38, 44, 45], which was discovered only in the FM state, and was found to be proportional to M . This is the first time that a non-zero AHE is reported in a non-centrosymmetric Weyl semimetal outside of a FM state.

Existing proposals for mechanisms responsible for AHE in AFM materials prove inadequate for the non-centrosymmetric SmAlSi. First principles calculations [40] demonstrate the possibility of non-zero AHE in AFM

* current affiliation: Department of Physics, Hong Kong University of Science and Technology, Clear Water Bay, Hong Kong, China

† corresponding author: E. Morosan emorosan@rice.edu

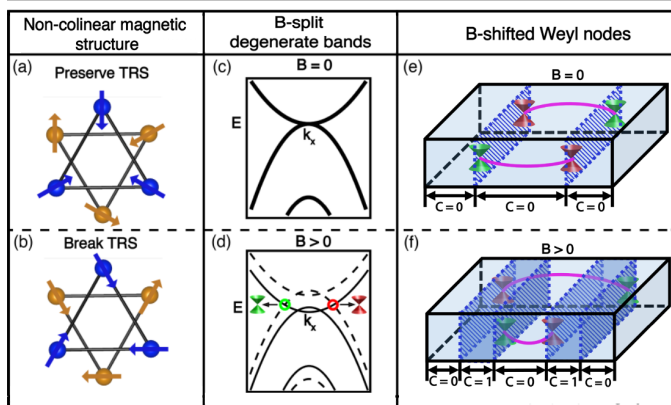


FIG. 1. Proposed AHE mechanisms in Mn_3Sn , GdPtBi and SmAlSi , based on (a-b) breaking T in non-collinear magnetic structures, (c-d) field-split degenerate bands, or (e-f) field-shifted Weyl nodes. (a-b) Comparison of two possible AFM magnetic structures in Mn_3Sn which forbid any finite AHE (a) or allow finite AHE (b). (c-d) Comparison of the GdPtBi band structure without (c) and with (d) applied magnetic field. The magnetic field lifts the band degeneracy and induces Weyl points. (e-f) Comparison of SmAlSi band structure without (e) and with (f) applied magnetic field. The Weyl nodes with different chiralities are illustrated in red and green, with Fermi arcs connecting them (magenta curves). The magnetic field changes the position of the Weyl nodes and induces a region with non-zero Chern number (c) in the Brillouin zone.

materials with non-collinear magnetic structures. The non-collinear magnetic structure can spontaneously break the time-reversal symmetry (T). In the AFM kagomé metal Mn_3Ir , breaking T results in non-zero Berry curvature and non-zero AHC. In the isostructural Mn_3Sn and Mn_3Ge , the Mn magnetic sublattice determines if T is broken, which, in turn, determines if there is non-zero AHE, as illustrated in Fig. 1(a-b). The magnetic structure in Fig. 1(a) is a bipartite lattice (antiparallel magnetic moment pairs) and preserves T , while the magnetic structure in Fig. 1(b) carries a winding chirality and break T . If the Weyl points are close to the Fermi energy E_F , the amplitude of the AHE is enhanced compared to cases where the Weyl points are away from E_F [46]. Overall, the broken T and the Weyl points created by the broken symmetry could explain the observation of the AHE in the ordered state of Mn_3Sn and Mn_3Ge [29, 30].

In stark contrast to Mn_3Sn and Mn_3Ge , neutron scattering and μSR measurements show that the magnetic order in GdPtBi is collinear AFM type below $T_N = 9.2$ K [12, 31]. Despite the lack of inversion center, the electronic structure of GdPtBi in zero field does not feature any Weyl nodes [12, 31]. However, AHE is observed up to 50 K, which is significantly larger than T_N . Despite these differences, the GdPtBi hosts non-trivial topology, similarly to Mn_3Sn and Mn_3Ge . By breaking T via an external magnetic field, the degeneracy of the electronic bands

is lifted through the exchange interaction between the Gd ions [11, 12]. As illustrated in Fig. 1(c-d), the combination of Zeeman effect and magnetic exchange interaction splits the electronic bands, leading to the formation of Weyl nodes in GdPtBi [11, 12]. This mechanism is responsible for the observed AHE as well as the anomalous Nernst effect, negative longitudinal magnetoresistance, and planar Hall effect in GdPtBi [11, 12, 31, 47, 48].

Weyl nodes can occur in non-centrosymmetric materials even in the absence of an applied magnetic field, as is the case in $\text{ReAl}(\text{Si},\text{Ge})$ [41, 42]. In T -breaking Weyl semimetals, if T is preserved, Weyl nodes with different chiralities appear at opposite momenta, and all regions in the first Brillouin zone have zero Chern number, such that the AHE is expected to be zero [Fig. 1(e)]. FM order spontaneously breaks T [41], and the Weyl nodes are effectively shifted by the exchange interaction, resulting in non-zero integration of the Berry curvature that leads to non-zero AHE. Here we extend this scenario to materials without FM order. An external magnetic field could break T , and the magnetic exchange interaction could act as FM exchange. As a result, there are regions with non-zero Chern number in the first Brillouin zone [Fig. 1(f)], leading to a field-induced non-zero AHE. It is worth noting that the Zeeman energy is typically significantly smaller than the magnetic exchange energy. Therefore, the AHE resulting from this mechanism is expected to be substantially smaller in NM materials compared to magnetic materials. In the magnetic system SmAlSi , we expect a nonzero AHE even in the PM state, particularly within the temperature range just above the Néel temperature T_N .

Our earlier work has shown that SmAlSi orders antiferromagnetically below $T_N = 11.3$ K, and undergoes a second magnetic transition at $T_1 = 4.1$ K [27]. Recent neutron scattering measurements by Yao *et al.* revealed the incommensurate AFM nature of the magnetic order below T_N [26]. Magnetic Bragg peaks were found at $\mathbf{Q} = (1/3-\delta, 1/3-\delta, 4)$ and $(1/3-\delta, 1/3-\delta, 8)$, which could be indexed by a propagation vector $\mathbf{k} = (1/3-\delta, 1/3-\delta, 0)$ with $\delta = 0.007(7)$. We also carried out diffraction measurements and confirmed the basic magnetic order wave vector is $(1/3, 1/3, 0)$ with an ordering temperature of $T_N = 11.2(2)$ K [Fig. S1(a,b)], where the uncertainty represents one standard deviation.

Magnetotransport measurements with current along the c/a axis and magnetic field parallel to the b axis revealed large anomalous Hall contributions to the resistivity and conductivity in both the AFM and PM states. The non-linear field-dependent Hall resistivity components ρ_{xz} and ρ_{zx} [Fig. 2(a,b)] indicate the coexistence of electron and hole carriers, consistent with previous studies [6, 38, 49], although these measurements were performed for a different current-field configuration ($j \parallel a$, $H \parallel c$). Surprisingly, the Hall resistivity ρ_{xz} and ρ_{zx} shows an unusual plateau between 0 and 2 T [Fig. 2(a,b), inset], which was not observed before, likely due to the different measurement configuration [6, 38, 49].

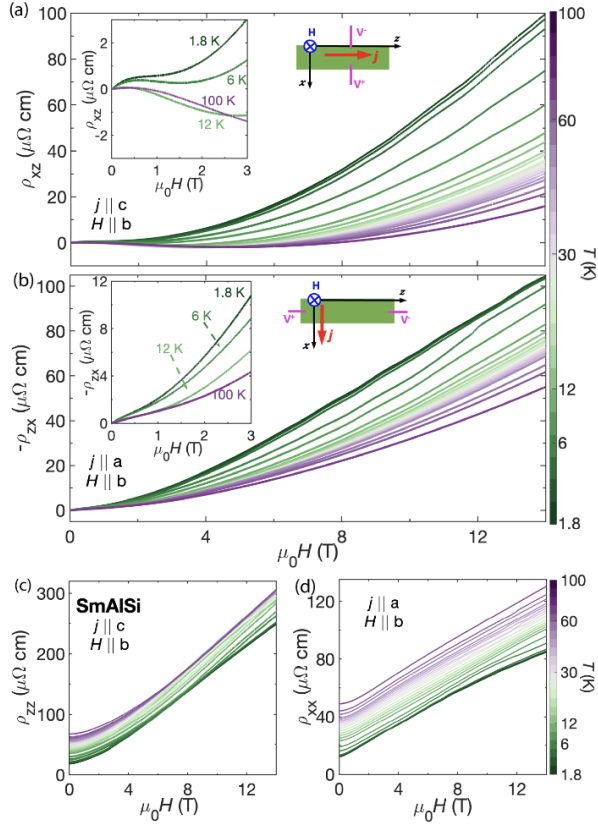


FIG. 2. Transverse resistivity (ρ_{xz} and ρ_{zx}) longitudinal resistivity (ρ_{zz} and ρ_{xx} of SmAlSi). (a, b) Field-dependent Hall resistivity ρ_{xz} and ρ_{zx} , with current $j \parallel c$ and magnetic field $H \parallel b$ (a) and current $j \parallel a$ and magnetic field $H \parallel b$ (b), respectively. The schematics of the corresponding Hall resistivity are shown in the inset. (c,d) Field-dependent resistivity ρ_{zz} and ρ_{xx} as a function of magnetic field.

Considering the additive Hall conductivity contributions [22], we use conductivity (rather than resistivity) analysis to probe the existence of the anomalous Hall effect. Since c axis is not equivalent to the a or b axis, the conductivity tensor and the resistivity tensor are connected through

$$\begin{bmatrix} \sigma_{xx} & \sigma_{xz} \\ \sigma_{zx} & \sigma_{zz} \end{bmatrix} = \frac{1}{\rho_{xx} * \rho_{zz} - \rho_{xz} * \rho_{zx}} \begin{bmatrix} \rho_{xx} & -\rho_{xz} \\ -\rho_{zx} & \rho_{zz} \end{bmatrix} \quad (1)$$

Fig. 2(a,b) shows the measured resistivity data for the relevant current (j) and field (H) orientations, which are used in eq. 1 to estimate the conductivity components σ_{xz} and σ_{zx} (Fig. 3(a,c)). The unusual plateau between 0 and 2 T in ρ_{xz} develops into an additional peak in σ_{xz} and a broad maximum in σ_{zx} .

To rule out a simple multi-band explanation for the observed magnetotransport, we performed two-band model fits to capture the low-field anomaly at 1.8 K. An example of such a fitting is shown in Fig. S5 (dashed lines) for $n_1 = 1.08 \cdot 10^{20} \text{cm}^{-3}$, $\mu_1 = 606 \text{cm}^2 \text{V}^{-1} \text{s}^{-1}$ and $n_2 = 5.36 \cdot 10^{17} \text{cm}^{-3}$, $\mu_2 = 30436 \text{cm}^2 \text{V}^{-1} \text{s}^{-1}$. However, the best fits do not capture the Hall conductivity

well for the entire field range. In addition, the conductivity from the fit $\sigma_{xx}^{fit}(H=0) = n_1 e \mu_1 + n_2 e \mu_2 = 1.31 \cdot 10^4 \Omega^{-1} \text{cm}^{-1}$ is significantly smaller than the experimental value $\sigma_{xx}(H=0) = 8.18 \cdot 10^4 \Omega^{-1} \text{cm}^{-1}$. These observations suggest that a simple multi-band model without the inclusion of an anomalous term is not adequate to account for the Hall conductivity.

For magnetic materials, the Hall conductivity sums up two contributions, if the topological spin texture is not considered: the ordinary Hall effect σ^N , and the AHE σ^A [22]:

$$\sigma_{xz} = \sigma_{xz}^N + \sigma_{xz}^A, \quad (2)$$

where the AHE is proportional to the magnetization M $\sigma_{xz}^A = S_H M$. Assuming the linear field dependence of the Hall resistivity, and a small Hall angle ($\rho_{xz} \ll \rho_{zz}$), the measured Hall resistivity ρ_{xz} can be written as:

$$\rho_{xz} = R_0 H + S_H \rho_{zz}^2 M. \quad (3)$$

While this formula has been successfully applied to analyze the AHE in many FMs, it fails to describe high-mobility multi-band systems. In GdPtBi for example, the field-dependent normal Hall effect is nonlinear due to the multi-band transport [12, 31]. Instead, the AHE is estimated by subtracting the scaled Hall resistivity measured far above the AFM ordering temperature ($T_N = 9.2 \text{K}$). Such analysis is valid assuming the carrier density and mobility only slightly vary below this temperature. This may not be the case for SmAlSi. To capture the nonlinear field dependence of the Hall effect, we performed a two-band fit to the high field Hall conductivity data σ_{xz} and σ_{zx} . Example fits are shown as dashed lines in Fig. 3(a,c). The difference between the data and model fits $-\sigma_{xz}^A$ [Fig. 3(b,d)] reflects the AHE contribution. A contour plot of this transport response in the $H - T$ phase diagram is shown in Fig. 4(a). Such AHE map bears a striking resemblance to that established for GdPtBi [12, 31]: both compounds display a peak at low fields, after subtracting the Hall conductivity fit to the high field data. Moreover, the peak persists far above the AFM transition temperature, although the amplitude is reduced with increasing T . In GdPtBi, the AHE persists up to $\sim 50 \text{K}$ when $T_N = 9.2 \text{K}$ [12, 31]. By comparison, it persists up to temperatures twice as high $T \sim 100 \text{K}$ in SmAlSi, even when the ordering temperature is comparable $T_N = 11.3 \text{K}$. At 1.8 K, σ_{xz}^A and σ_{zx}^A reach 1380 and $1030 \Omega^{-1} \text{cm}^{-1}$, about one order of magnitude larger than the values in GdPtBi ($\sim 30 - 200 \Omega^{-1} \text{cm}^{-1}$). The resulting tangent of the anomalous Hall angle, $\tan \theta_{xz}^A = \sigma_{xz}^A / \sigma_{xx}$ is 0.017 and $\tan \theta_{zx}^A = \sigma_{zx}^A / \sigma_{zz}$ is 0.02 , which is about 1/8 to 1/10 of that observed in GdPtBi [12, 31], but comparable to that of CeAlSi (0.02) or PrAlGe (0.025) [38, 50], although the latter systems are both ferromagnets.

Compared with results from [26] where the Hall anomaly is reported in the finite-field A phase, the Hall anomaly from our Hall conductivity data is found in a

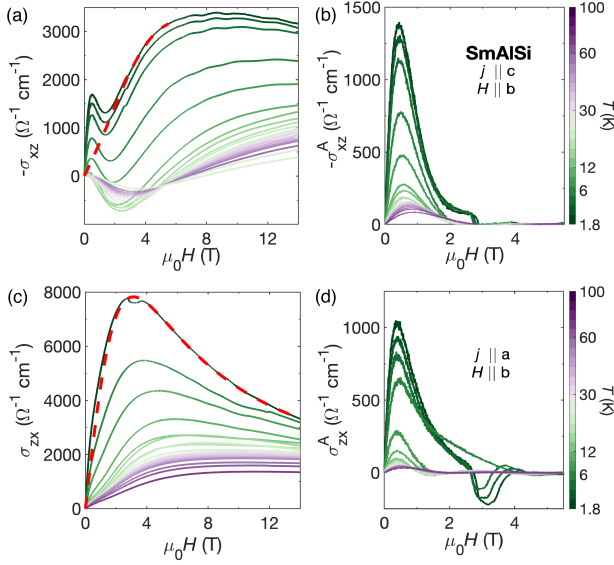


FIG. 3. The AHC of SmAlSi. (a,c) Field-dependent Hall conductivity σ_{xz} and σ_{zx} of SmAlSi. The red dashed lines are the two-band fit ordinary Hall contribution to the Hall conductivity at 1.8 K. (b,d) AHC σ_{xz}^A and σ_{zx}^A as a function of the magnetic field at different temperatures $T = 1.8$ K to 100 K.

much larger temperature range and a distinct magnetic field range. In addition to a different measurement geometry (different current and field direction), the measurements are done on two different samples with better crystal quality (as demonstrated by heat capacity [27] and quantum oscillations data (SI Figs. 7-8)). In addition, the differences in the quantum oscillation frequencies and Hall resistivity indicate that the Fermi energy in our samples is lower than in the samples from [26].

The contour map of the AHE contribution in SmAlSi [Fig. 4(a)] shows a striking resemblance to that in GdPtBi [31]. Weyl nodes are expected to play an important role in both systems. Nevertheless, the mechanisms for the formation of the Weyl nodes are quite different. The electronic structure of GdPtBi in zero field does not feature any Weyl nodes. Under a finite field, Weyl nodes form due to the field-induced Zeeman splitting combined with the effect of AFM exchange field. Recently, an AHE with an amplitude much larger than GdPtBi was discovered in TbPdBi [47]. The study proposed a crossover from a Berry phase cancellation in the AFM/PM state to a half-topological state with large non-zero Berry curvature (hosted by anti-crossing points) in the FM state based on the band structure calculation [47]. The Berry curvature in the reciprocal space is responsible for the AHE in both compounds. The formation of the anti-crossing points in TbPdBi is similar to the Weyl points in GdPtBi: exchange field of the RE ions in the corresponding compounds. In contrast, the Weyl nodes in SmAlSi exist even at zero field above T_N , due to I breaking and SOC.

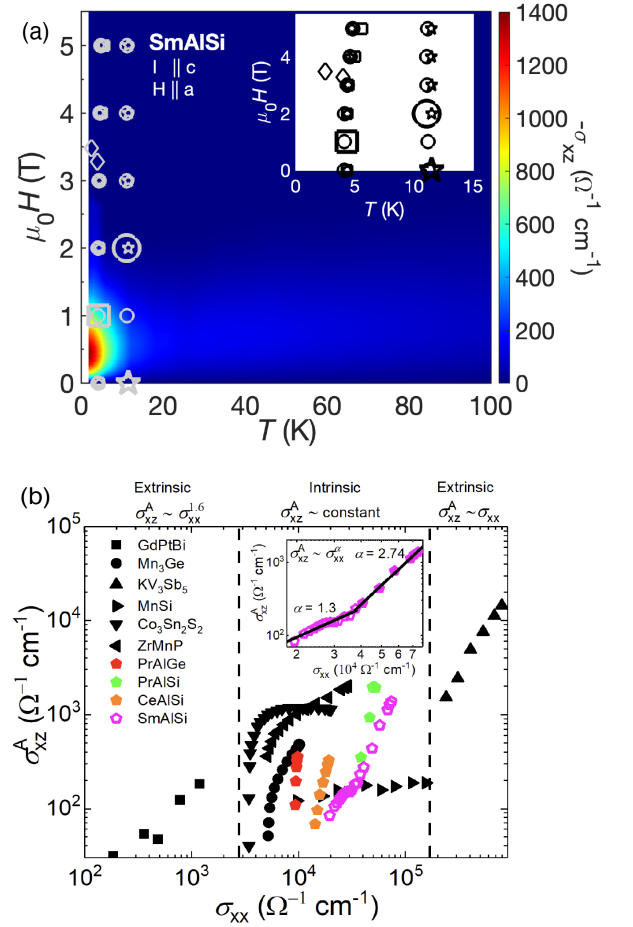


FIG. 4. (a) Contour map of σ_{xz}^A for $\mu_0H = 0 - 14$ T and $T = 1.8 - 100$ K. The symbols are the phase boundaries determined from Figs. S1-3. Inset: a zoomed-in view of the phase diagram at low temperatures. The phase boundaries are determined from the peaks in $C_p(T)$ (stars), $d(M(T)/H)/dT$ (squares), $d\rho(T)/dT$ (circles), $dM(H)/dH$ (diamonds). (b) σ_{xz}^A vs. σ_{xx} for SmAlSi (magenta pentagons), other RAl(Si,Ge) (red, green, and orange pentagons) [38, 44, 45], and other topological semimetals (black symbols) [16, 29, 31, 32, 36, 37].

The AHE in SmAlSi is also significantly different from that in $Mn_3(Ge, Sn)$. In the latter, AHE is observed below the ordering temperature while in the former, it persists well above T_N . At $H = 0$, the AHE is zero in SmAlSi and non-zero in $Mn_3(Ge, Sn)$. These differences highlight the importance of the magnetic order in $Mn_3(Ge, Sn)$ to induce the AHE, which spontaneously breaks T , while in SmAlSi, it is the magnetic field that breaks T .

It is necessary to discuss possible Fermi surface reconstruction under a magnetic field in the presence of AHE, as discovered in $YbMnBi_2$ [51]. In $YbMnBi_2$, it has been proposed that the canted Mn moments could change the shape and position of the bands dramatically, such that the energy of the Weyl points relative to the Fermi energy can be tuned, and, in turn, tune the intrinsic anomalous Hall and Nernst effects [51]. It should be noted that the

magnetic exchange energy in YbMnBi₂ is significantly higher than in SmAlSi: $\mu_{eff}^{Mn} \sim 4 \mu_B$ with $T_N = 290$ K, and $\mu_{eff}^{Sm} \sim 0.85 \mu_B$ with $T_N = 11.3$ K, respectively. The exchange energy from the canted Sm³⁺ ions should be too small to significantly impact the Fermi surface topology as in YbMnBi₂. In addition, the quantum oscillation frequencies [Fig. S8] do not change across the transitions. Therefore, neither temperature nor field are likely to induce Fermi surface reconstruction in SmAlSi.

We benchmark the AHC in SmAlSi against other established topological semimetals, as indicated by the σ_{xz}^A dependence on σ_{xx} [Fig. 4(b)]. The conductivity of SmAlSi falls in the intrinsic regime, where the interband-coherence-driven intrinsic AHC is independent of the electron scattering mean free time, and should be a constant: $\sigma_{xz}^A \sim \text{constant}$. The amplitude of the AHC is comparable to that of other materials with intrinsic AHE.

The extrinsic skew scattering may contribute to the AHE in SmAlSi as well. In YbMnBi₂, the strong anisotropy of the Fermi surface leads to large anisotropy in the conductivity ($\sigma_{bb}/\sigma_{cc} \sim 35$). With H parallel to a, the anomalous Hall and Nernst effects are dramatically enhanced when the current or temperature gradient is parallel to b, as expected for the extrinsic mechanism. In SmAlSi, the conductivity anisotropy is small ($\sigma_{zz}/\sigma_{xx} \sim 1.5$), with similar anomalous Hall conductivity amplitude $\sigma_{xz}^A \sim 1380 \Omega^{-1} \text{cm}^{-1}$ and $\sigma_{xx}^A \sim 1030 \Omega^{-1} \text{cm}^{-1}$.

Apart from the AHE, a non-coplanar spin texture may yield spin chirality, generating Hall anomaly that is usually referred to as THE [52]. We will elaborate on this scenario in the AFM and PM phases of SmAlSi.

Based on the current understanding, it is unclear if any magnetic phases have spin chirality in SmAlSi. Due to the large Sm neutron absorption cross section, neutron scattering experiments from [26] and this work only show the basic magnetic order wave vector as (1/3, 1/3, 0) with the magnetic structure undetermined, while the large standard deviation precludes a solid proof of incommensurate order. Moreover, the multi-q feature is missing in the neutron scattering results on SmAlSi, which has been seen as key evidence for non-coplanar spin texture. It is unclear if the magnetic structure establishes spin chirality in SmAlSi as host of skyrmionic correlation.

Skyrmionic correlation could also persist in a small temperature range outside the skyrmion phase, resulting in a vestigial skyrmion lattice phase, as has been shown in MnSi recently [53]. The vestigial phase is limited to a small range close to the skyrmion phase in MnSi, while the Hall anomaly persists in a much larger range well above the ordering temperature. Therefore, it is unlikely that the Hall anomaly in SmAlSi is related to the vestigial skyrmion lattice.

We now turn to the discussion of thermal fluctuations, which, in addition to long-range magnetic order, have been shown to yield finite spin chirality [54, 55]. A competition of thermal fluctuations and Zeeman energy or Dzyaloshinskii-Moriya (DM) interaction has been shown

to induce spin chirality in Gd₃Ru₄Al₁₂, and in thin film of SrRuO₃ and V-doped Bi₂Se₃, respectively [54, 55]. However, as proposed in [55], the fluctuation-driven effect is promoted only when the spin chirality between neighboring plaquettes is not canceled. For lattice motifs with equivalent polygons as in SmAlSi, the fluctuation-driven chirality is expected to cancel out.

It would therefore appear that none of the aforementioned mechanisms are adequate to describe the magnetotransport in SmAlSi. It will be helpful to further explore both the intrinsic and extrinsic contributions to the AHE in SmAlSi, as well as the magnetic structures and magnetic interactions through different theoretical and experimental approaches. The AHE in SmAlSi [Fig. 4(b)] is not a constant as expected for intrinsic deflection [22]. Such behavior is similar to the AHE found in the FMs CeAl(Si,Ge) and PrAl(Si,Ge) [4, 38, 44, 45], despite the fact that the AHE is missing in their PM state. Here we provide a qualitative explanation of this dependence, based on a new mechanism.

In our proposed mechanism, the Weyl nodes evolution under an external magnetic field can generate non-zero AHE in non-centrosymmetric systems. Moreover, the AHC has been shown to be proportional to the momentum space separation between Weyl nodes of different chiralities [39]. In SmAlSi, such separation is directly related to the size of the magnetic interaction between the canted Sm³⁺ magnetic moments. A larger moment will induce a larger shift in the electronic bands. The size of the canted moment is reflected in the susceptibility [Fig. S3(a)] or the isothermal magnetization [Fig. S3(c)]. The measurements of both quantities show a negative dependence on temperature, which is consistent with the change in the AHE.

Moreover, the σ_{xz}^A of SmAlSi exhibits two regions that could be differentiated by distinct power-law coefficients, as illustrated by the linear fits in the inset of Fig. 4(b). These two regions coincide with the PM phase (full symbols) and the AFM phase (open symbols). To quantitatively explain this unconventional power-law behavior, extensive theory and experimental work are required to study the AHE dependence under this new mechanism.

We discovered large AHE in both the AFM and PM states of SmAlSi, which is the first observation of AHE in the non-FM state of non-centrosymmetric Weyl semimetals. We propose a new AHE mechanism in non-centrosymmetric Weyl semimetals, based on an external magnetic field breaking T , and shifting the position of the Weyl nodes. Consequently, these Weyl nodes create regions with non-zero Chern number and generate AHE. Our work motivates further studies into the quantitative understanding of the AHE in SmAlSi and other AFM materials.

This work was primarily supported by the Department of Defense, Air Force Office of Scientific Research under Grant No. FA9550-21-1-0343. S.L. and E.M. acknowledge partial support from the the Robert A. Welch Foundation grant C-2114. K.T.L. acknowledges the support

of HKRGC through RFS2021-6S03, C6025-19G, AoE/P-701/20, 16307622, 16310520 and 16310219. A portion of this research used resources at the High Flux Isotope Reactor, a DOE Office of Science User Facility operated by the Oak Ridge National Laboratory. The work of EMC (neutron scattering data collection and analysis) was sup-

ported by the U.S. Department of Energy (DOE), Office of Science, Basic Energy Sciences (BES), Materials Sciences and Engineering Division. The identification of any commercial product or trade name does not imply endorsement or recommendation by the National Institute of Standards and Technology.

-
- [1] Fujishiro, Y., et al., Giant anomalous Hall effect from spin-chirality scattering in a chiral magnet. *Nat. Commun.* **12**, 317 (2021).
- [2] Yang, H., et al., Topological Weyl semimetals in the chiral antiferromagnetic materials Mn₃Ge and Mn₃Sn. *New J. Phys.* **19**, 015008 (2017).
- [3] Liu, D. F., et al., Magnetic Weyl semimetal phase in a Kagomé crystal. *Science* **365**(6459), 1282-1285 (2019).
- [4] Puphal, P., et al., Topological Magnetic Phase in the Candidate Weyl Semimetal CeAlGe. *Phys. Rev. Lett.* **124**, 017202 (2020).
- [5] Dzsaber, S., et al., Giant spontaneous Hall effect in a nonmagnetic Weyl-Kondo semimetal. *PNAS* **118**(8), e2013386118 (2021).
- [6] Gaudet, J., et al., Weyl-mediated helical magnetism in NdAlSi. *Nat. Mater.* **20**, 1650-1656 (2021).
- [7] Lishitz, R., Magnetic point groups and space groups. *arXiv: 0406675* (2022).
- [8] Watanabe, H., Po, H. and Vishwanath, A., Structure and topology of band structures in the 1651 magnetic space groups. *Sci. Adv.* **4**, eaat8685 (2018).
- [9] Jennifer, C., Bradlyn, B., and Vergniory, M. G., Multifold nodal points in magnetic materials. *APL Mater.* **7**, 101125 (2019).
- [10] Wang, J., et al., NdAlSi: a magnetic Weyl semimetal candidate with rich magnetic phases and atypical transport. *Phys. Rev. B* **105**, 144435 (2022).
- [11] Hirschberger, M., et al., The chiral anomaly and thermopower of Weyl fermions in the half-Heusler GdPtBi. *Nat. Mater.* **15**, 1161-1165 (2016).
- [12] Shekar, C., et al., Anomalous Hall effect in Weyl semimetal half-Heusler compounds RPtBi: (R = Gd and Nd). *PNAS* **115**(37), 9140-9144 (2018).
- [13] Sanchez, D., et al., Observation of Weyl fermions in a magnetic non-centrosymmetric crystal. *Nat. Commun.* **11**, 3356 (2020).
- [14] Morali, N., et al., Fermi-arc diversity on surface terminations of the magnetic Weyl semimetal Co₃Sn₂S₂. *Science* **11**, 3356 (2019).
- [15] Li, P., et al., Giant room temperature anomalous Hall effect and tunable topology in a ferromagnetic topological semimetal Co₂MnAl. *Nat. Commun.* **11**, 3476 (2020).
- [16] Liu E., et al., Giant anomalous Hall effect in a ferromagnetic kagome-lattice semimetal. *Nat. Phys.* **14**, 1125-1131 (2018).
- [17] Feng, J., Pashley, R. and Nicolet, M., Magnetoelectric properties of magnetite thin films. *J. Phys. C: Solid State Phys.* **8**, 1010 (1975).
- [18] Taguchi, Y., et al., The spin chirality induced anomalous Hall effect in pyrochlore ferromagnets. *J. Phys.: Condens. Matter* **16**, S599 (2004).
- [19] Chun, S. H., et al., Interplay between Carrier and Impurity Concentrations in Annealed Ga_{1-x}Mn_xAs: Intrinsic Anomalous Hall Effect. *Phys. Rev. Lett.* **99**, 086602 (2007).
- [20] Miyasato, T., et al., Crossover Behavior of the Anomalous Hall Effect and Anomalous Nernst Effect in Itinerant Ferromagnet. *Phys. Rev. Lett.* **99**, 086602 (2007).
- [21] Shiomi, Y., Onose, Y., and Tokura, Y., Extrinsic anomalous Hall effect in charge and heat transport in pure iron, Fe_{0.97}Si_{0.03}, and Fe_{0.97}Co_{0.03}. *Phys. Rev. B* **79**, 100404 (2009).
- [22] Nagaosa, N., et al., Anomalous Hall effect. *Rev. Mod. Phys.* **82**, 1539 (2010).
- [23] Tian, L., et al., Anomalous Hall effect in ZrTe₅. *Nat. Phys.* **14**, 451-4554 (2018).
- [24] Armitage, N. P., Mele, E.J. and Vishwanath, A., Weyl and Dirac semimetals in three-dimensional solids. *Rev. Mod. Phys.* **90**, 015001 (2018).
- [25] Jin, H., et al., Transport of Topological Semimetals. *Annu. Rev. Mater. Res.* **49**, 207-252 (2019).
- [26] Yao, X., et al., Topological spiral magnetism in the Weyl semimetal SmAlSi. *Phys. Rev. X* **13**, 011035 (2023).
- [27] Zhang, Y., et al., Kramers Nodal Lines and Weyl Fermions in SmAlSi. *Commun. Phys.* **6**, 134 (2023).
- [28] Zeng, C., et al., Linear Magnetization Dependence of the Intrinsic Anomalous Hall Effect. *Phys. Rev. Lett.* **96**, 037204 (2006).
- [29] Nayak, A. K., et al., Large anomalous Hall effect driven by a nonvanishing Berry curvature in the noncolinear antiferromagnet Mn₃Ge. *Sci. Adv.* **2**, e1501870 (2016).
- [30] Nakatsuji, S., Kiyohara, N. and Higo, T., Large anomalous Hall effect in a non-collinear antiferromagnet at room temperature. *Nature* **527**, 212-215 (2016).
- [31] Suzuki T., et al., Large anomalous Hall effect in a half-Heusler antiferromagnet. *Nat. Phys.* **12**, 1119-1123 (2016).
- [32] Lee, M., et al., Hidden constant in the anomalous Hall effect of high-purity magnet MnSi. *Phys. Rev. B* **75**, 172403 (2007).
- [33] Wang, Q., et al., Anomalous Hall effect in a ferromagnetic Fe₃Sn₂ single crystal with a geometrically frustrated Fe bilayer kagome lattice. *Phys. Rev. B* **94**, 075135 (2016).
- [34] Guin, S. N., et al., 2D-Berry-Curvature-Driven Large Anomalous Hall Effect in Layered Topological Nodal-Line MnAlGe. *Adv. Mater.* **33**, 2006301 (2021).
- [35] Kim K., et al., Large anomalous Hall current induced by topological nodal lines in a ferromagnetic van der Waals semimetal. *Nat. Mater.* **17**, 794-799 (2018).
- [36] Singh, S., et al., Anisotropic Nodal-Line-Derived Large Anomalous Hall Conductivity in ZrMnP and HfMnP. *Adv. Mater.* **33**, 2104126 (2021).
- [37] Yang, S. Q., et al., Giant, unconventional anomalous Hall effect in the metallic frustrated magnet candidate, KV₃Sb₅. *Sci. Adv.* **6**, eabb6003 (2020).

- [38] Destraz, D. Q., et al., Magnetism and anomalous transport in the Weyl semimetal PrAlGe: possible route to axial gauge fields. *npj Quantum Materials* **5**, 5 (2020).
- [39] Burkov, A. A., Anomalous Hall Effect in Weyl Metals. *Phys. Rev. L* **113**, 187202 (2014).
- [40] Chen, H., Niu, Q. and MacDonald, A. H., Anomalous Hall Effect Arising from Noncollinear Antiferromagnetism. *Phys. Rev. L* **112**, 017205 (2014).
- [41] Chang G., et al., Magnetic and noncentrosymmetric Weyl fermion semimetals in the RAlGe family of compounds (R = rare earth). *Phys. Rev. B* **97**, 041104(R) (2018).
- [42] Xu SY., et al., Discovery of Lorentz-violating type II Weyl fermions in LaAlGe. *Sci. Adv.* **3**, e1603266 (2019).
- [43] Suzuki T., et al., Singular angular magnetoresistance in a magnetic nodal semimetal. *Science* **365**, 377-381 (2019).
- [44] Yang, H., et al., Noncollinear ferromagnetic Weyl semimetal with anisotropic anomalous Hall effect. *Phys. Rev. B* **103**, 115143 (2021).
- [45] Meng, L., et al., Nonsaturating magnetoresistance, anomalous Hall effect, and magnetic quantum oscillations in the ferromagnetic semimetal PrAlSi. *Phys. Rev. B* **102**, 085143 (2020).
- [46] Kübler, J. and Felser, C., Non-collinear antiferromagnets and the anomalous Hall effect. *EPL* **108**, 67001 (2014).
- [47] Zhu, Y., et al., Large anomalous Hall effect and negative magnetoresistance in half-topological semimetals. *Commun. Phys.* **6**, 346 (2023).
- [48] Liang, S., et al., Experimental Tests of the Chiral Anomaly Magnetoresistance in the Dirac-Weyl Semimetals Na₃Bi and GdPtBi. *Phys. Rev. X* **8**, 031002 (2018).
- [49] Cao, W., et al., Quantum oscillations in noncentrosymmetric Weyl semimetal SmAlSi. *Chin. Phys. Lett* **39**, 047501 (2022).
- [50] Cheng, E., et al., Anomalous transverse transport and phase transitions in Weyl semimetals RAlSi (R = La, Ce). *arxiv:2301.03800* (2023).
- [51] Pan, Y., et al., Giant anomalous Nernst signal in the antiferromagnet YbMnBi₂. *Nat. Mater.* **21**, 203-209 (2022).
- [52] Tokura, Y. and Kanazawa, N., Magnetic skyrmions materials. *Chem. Rev.* **121**, 2857-2897 (2021).
- [53] Kindervater, J., et al., Weak Crystallization of Fluctuating Skyrmion Textures in MnSi. *Phys. Rev. X* **9**, 041059 (2019).
- [54] Wang, W., et al., Spin chirality fluctuation in two-dimensional ferromagnets with perpendicular magnetic anisotropy. *Nat. Mater.* **18**, 1054-1059 (2019).
- [55] Kolincio, K., et al., Kagome Lattice Promotes Chiral Spin Fluctuations. *Phys. Rev. Lett.* **130**, 136071 (2023).

Supplementary information: Anomalous Hall effect emerging from field-induced Weyl nodes in SmAlSi

Yuxiang Gao,^{1,2} Shiming Lei,^{1,3,*} Eleanor M. Clements,^{4,5} Yichen Zhang,^{1,2} Xue-Jian Gao,⁶ Songxue Chi,⁷ Kam Tuen Law,⁶ Ming Yi,^{1,2} Jeffrey W. Lynn,⁴ and Emilia Morosan^{1,2,†}

¹*Department of Physics and Astronomy, Rice University, Houston, Texas 77005, USA*

²*Rice Center for Quantum Materials, Rice University, Houston, Texas 77005, USA*

³*Rice Center for Quantum Materials (RCQM) and Smalley-Curl Institute (SCI), Rice University, Houston, Texas 77005, USA*

⁴*NIST Center for Neutron Research, National Institute of Standards and Technology, Gaithersburg, Maryland 20899, USA*

⁵*Materials Science and Technology Division, Oak Ridge National Laboratory, Oak Ridge, Tennessee 37831, USA*

⁶*Department of Physics, Hong Kong University of Science and Technology, Clear Water Bay, Hong Kong, China*

⁷*Neutron Scattering Division, Oak Ridge National Laboratory, Oak Ridge, Tennessee 37831, USA*

(Dated: August 27, 2024)

I. NEUTRON SCATTERING

The wave vector for the magnetic ordering has previously been determined to be close to $(1/3, 1/3, 0)$, possibly slightly incommensurate with a value of $(1/3-\delta, 1/3-\delta, 0)$ with $\delta = 0.007(7)$ [1]. We chose coarse collimation of $48'-40'-40'-120'$ full-width-at-half-maximum to maximize the intensity, and consequently did not address the incommensurability issue. Initial exploratory measurements indicated that the signal-to-noise was somewhat better utilizing an energy of 14.7 meV; even though the absorption is higher, this was compensated by the higher Bragg peak structure factor. The quantitative determination of the magnetic structure(s) was prohibited by the very high Sm absorption. Fig. S1(a) shows the observed magnetic peak for the $(2/3, 2/3, 2)$ reflection, which turned out to be strongest given the shape of the crystal. In Fig. S1(b), the two magnetic transitions at $T_N = 11.3$ K and $T_1 = 4.1$ K are visible in the temperature dependence of the intensity of the $(2/3, 2/3, 2)$ peak (circles, left axis) and the magnetization derivative $d(\text{MT})/dT$ (solid line, right axis).

The black solid curve is a fit using mean field theory, from which the estimated ordering temperature is $T_N = 11.6(2)$ K. We noted that the data appeared to have some extra intensity below the lower transition at $T_1 = 4.7$ K, which may have a structural component but is currently not fully identified. We therefore restricted the fit to temperatures above 5 K. It is clear that mean field theory (or other typical order parameter models) does not adequately represent the observed temperature dependence of the data in the low temperature regime, which is quite different from the data in the inset to figure 2a in [1]. This indicates that there is additional magnetic intensity associated with this low temperature transition. The temperatures of the two transitions identified in neutron scattering measurements are consistent with our magnetization measurements (blue line in Fig. S1(b)).

* Current affiliation: Department of Physics, Hong Kong University of Science and Technology, Clear Water Bay, Hong Kong, China

† corresponding author: E. Morosan emorosan@rice.edu

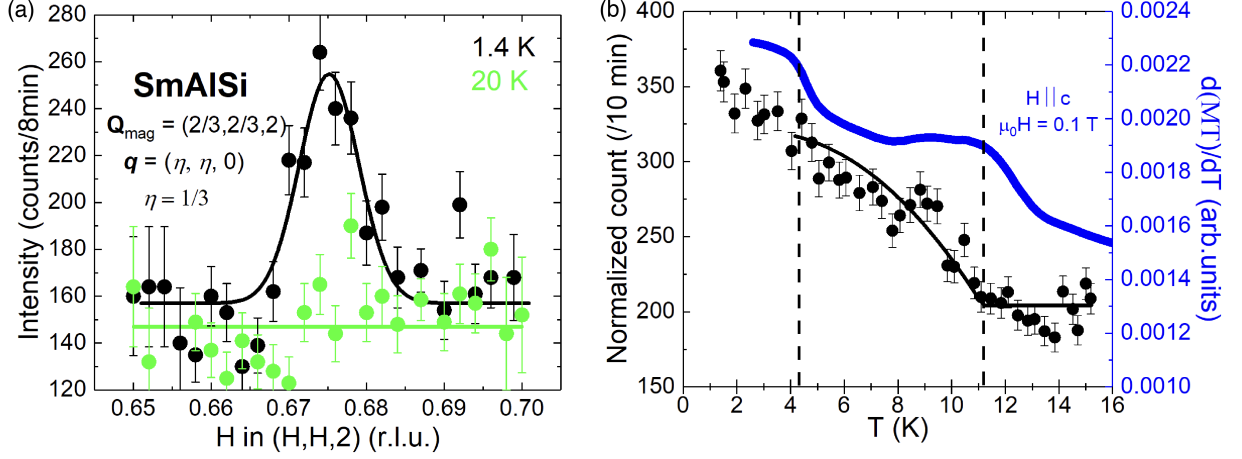


FIG. S1. Elastic neutron scattering of SmAlSi. (a) Neutron diffraction scan along $(H,H,2)$ direction. (b) Temperature dependence of the Bragg peak intensity (dots) and the mean field fit to the intensity (line). The blue line is $d(MT)/dT$ for $H \parallel c$ and $\mu_0H = 0.1$ T. Error bars represent one standard deviation.

II. PHASE DIAGRAM DETERMINATION

The magnetic phase diagram of SmAlSi is determined from electrical resistivity [Fig. S2], magnetization [Fig. S3] and heat capacity measurements [Fig. S4]. The phase boundaries in Fig. 4(b) are determined from the corresponding peaks in heat capacity [Fig. S4] and the derivatives of resistivity and magnetization [Fig. S2(b), Fig. S3(b,c)].

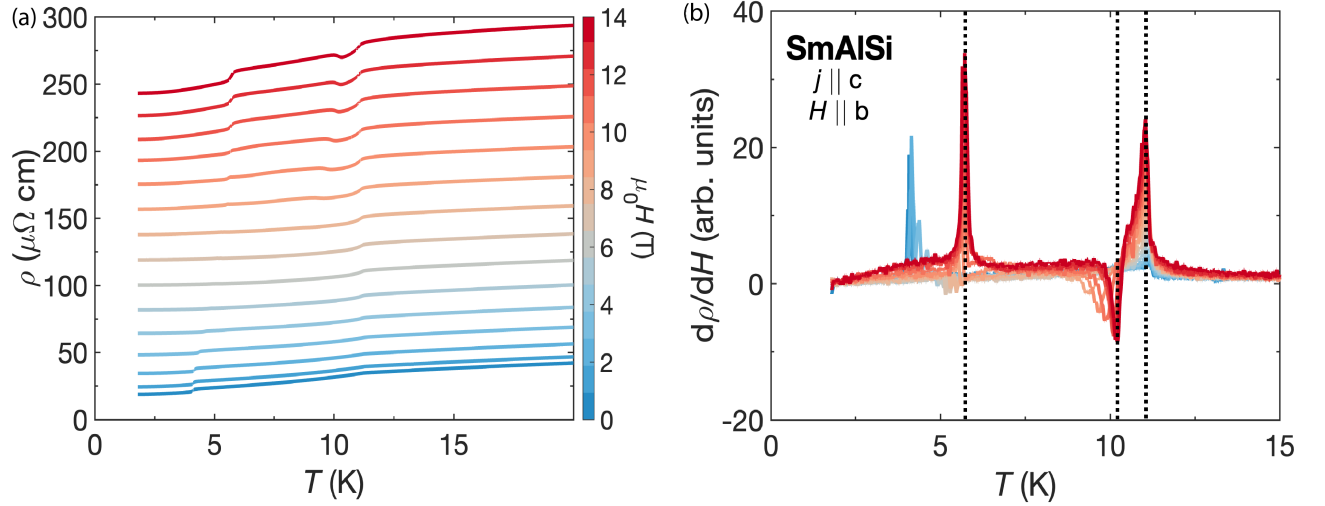


FIG. S2. Temperature-dependent resistivity ρ_{zz} , with current $j \parallel c$ and magnetic field $H \parallel b$. The circles in Fig. 4(b) are determined from the maxima and minima in $d\rho/dT$.

III. HALL EFFECT

The geometry for the Hall resistivity measurements ρ_{xz} and ρ_{zx} are shown in the inset of Fig. 2(a,b). According to the axes definition in Fig. 2(a,b), $\rho_{xz} = (V_x^+ - V_x^-) * t/I$ and $\rho_{zx} = (V_z^+ - V_z^-) * t/I$, where $V^{+/-}$ refers to the voltage, I is the current and t is the thickness of the sample. The data in the main text and supplementary materials are presented such that the positive (negative) sign of the signal reflects the positive (negative) sign of $V^+ - V^-$ as defined in Fig. 2(a,b). Therefore, $-\sigma_{xz}$ and $-\rho_{zx}$ are shown instead of σ_{xz} and ρ_{zx} .

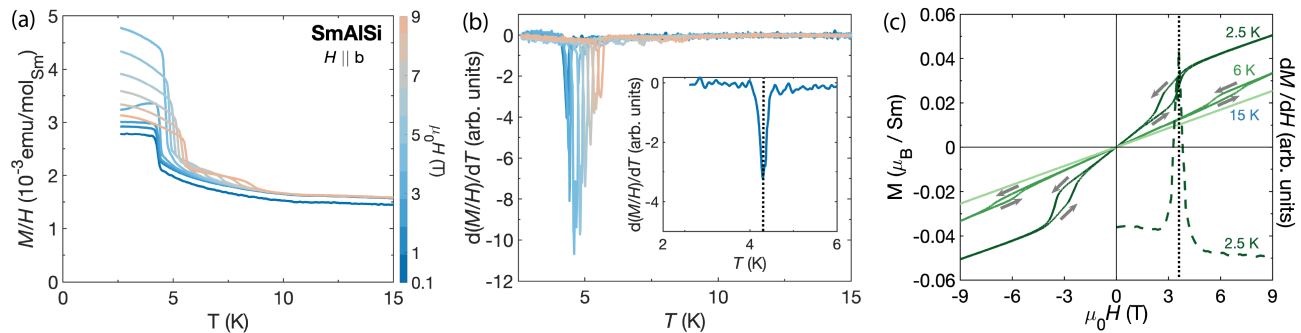


FIG. S3. (a) Temperature dependent susceptibility M/H with magnetic field $H \parallel b$. (b) Derivative of the M/H (a) as a function of temperature. (c) Magnetization as a function of field. The arrows indicate the field-swept direction. The dashed line is the derivative dM/dH at 2.5 K. The squares and diamonds in Fig. 4(a) are determined from the minima in $d(M/H)/dT$ and the maxima in dM/dH as in (c), respectively.

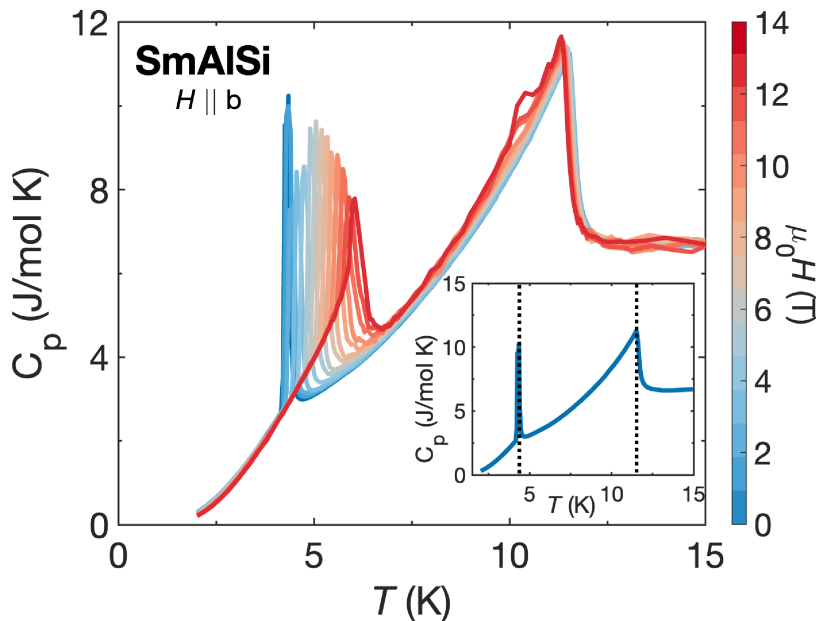


FIG. S4. Temperature dependent heat capacity C_p with magnetic field $H \parallel b$. The stars in Fig. 4(b) are determined from the peak positions.

A two-band model fit attempting to capture the low field anomaly in σ_{xz} is shown in Fig. S5. As discussed in the main text, the fit does not capture the Hall conductivity well, and the resulting longitudinal conductivity σ_{xx} is significantly lower than the σ_{xx} from measurements, which suggests that a simple multi-band model is not an adequate description of the Hall conductivity.

The normal Hall effect is extracted through a two-band model fitting to the high field range ($\mu_0 H \geq 2.5$ T). These fits reveal the coexistence of a hole pocket and an electron pocket. The carrier concentration and carrier mobility from the fits are shown in Fig. S6. Both the carriers concentrations and mobility are nearly temperature-independent, implying that the Fermi surface of SmAlSi does not undergo reconstruction.

IV. QUANTUM OSCILLATIONS

Shubnikov-de Haas (SdH) oscillations are used to understand the Fermi surface and how it changes with temperature. The oscillation frequency F from QO measurements is related to the extremal cross-sectional area A_k of the FS perpendicular to the applied magnetic field via the Onsager relation: $F = (\hbar A_k)/(2\pi e)$, where \hbar is the reduced Planck constant and e is the electron charge. The angular evolution of the QO frequency reflects the change of the

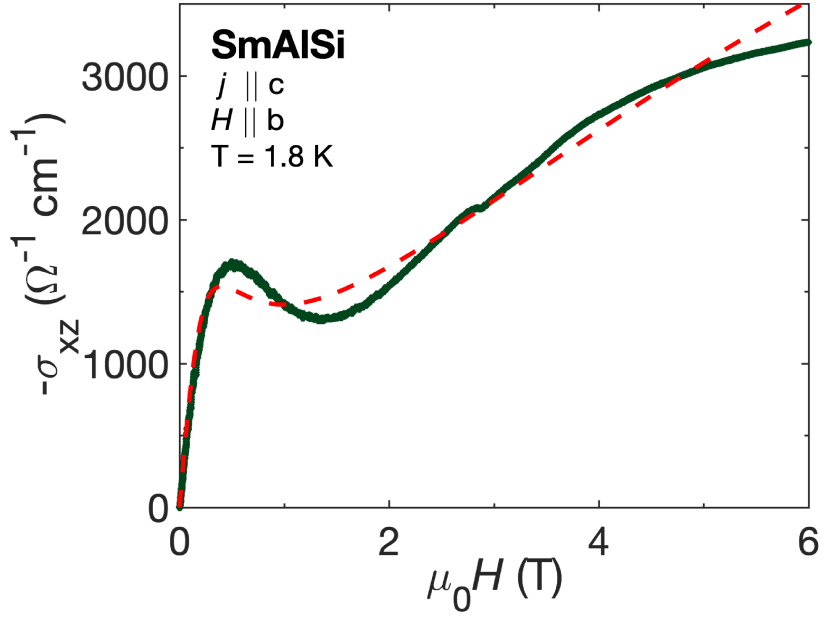


FIG. S5. Two band model fitting to low field ($\mu_0 H \leq 2.5$ T) of σ_{xz} at 1.8K with $n_1 = 1.08 \cdot 10^{20} \text{cm}^{-3}$, $\mu_1 = 606 \text{cm}^2 \text{V}^{-1} \text{s}^{-1}$ and $n_2 = 5.36 \cdot 10^{17} \text{cm}^{-3}$, $\mu_2 = 30436 \text{cm}^2 \text{V}^{-1} \text{s}^{-1}$.

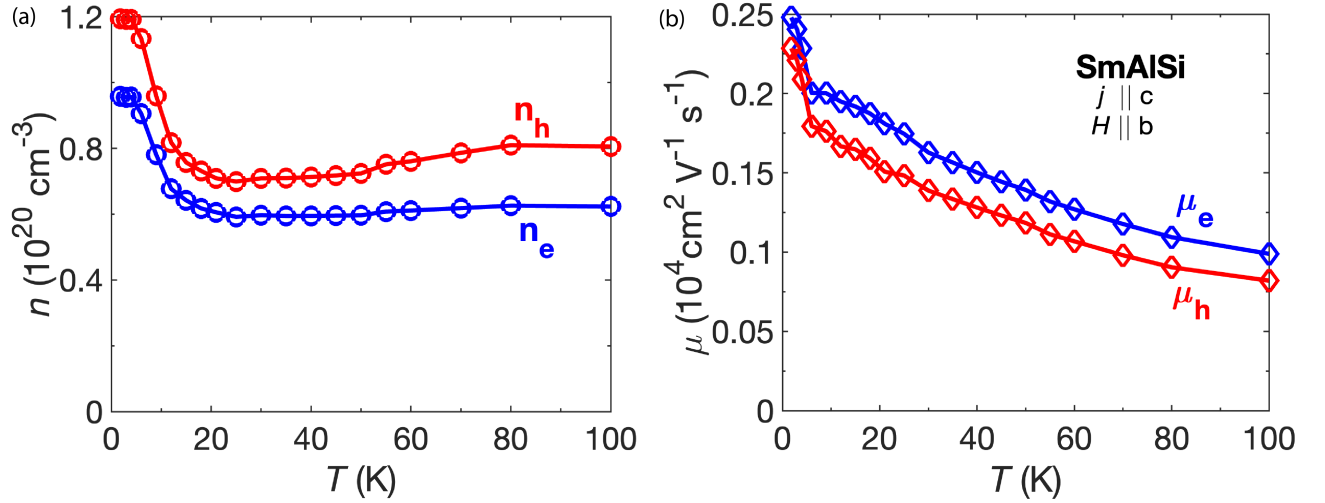


FIG. S6. The carrier concentration n_e , n_h and carrier mobility μ_e , μ_h extracted from the two-band model fitting on the Hall conductivity σ_{xz} to high fields ($\mu_0 H \geq 2.5$ T) as a function of temperature.

extreme orbits as the sample rotates relative to the magnetic field direction, while the change in QO frequency with temperature indicates a change in the extremal FS cross section, and might indicate a non-trivial FS topology. For both sets of measurements, the current is applied along the a direction, and the field is kept within the bc plane during the rotation for angle-dependent measurements. An illustration of the angle-dependent measurement configuration is shown in the inset of Fig. S7(a).

We measured the SdH oscillations at different temperatures, and the background-subtracted results are shown in Fig. S8(a,b). The oscillation amplitude is lower at higher temperatures, as expected. The frequency peaks in the FFT spectra are labeled according to the definition in Fig. S7 (e,f) [2]. The QO frequencies do not change across the magnetic transition temperatures T_N and T_1 . Instead, a gradual change in the frequencies in the FFT spectrum is found above 15 K, which is higher than T_N . This is uncommon since the FS reconstruction is not expected in the paramagnetic state.

It should be noted that a similar shift has been found in previous SmAlSi studies [3], and also in the isostructural NdAlSi [4]. In Fig. 4(b, c) of [4] it can be seen that the QO frequencies are also shifting within the same magnetic

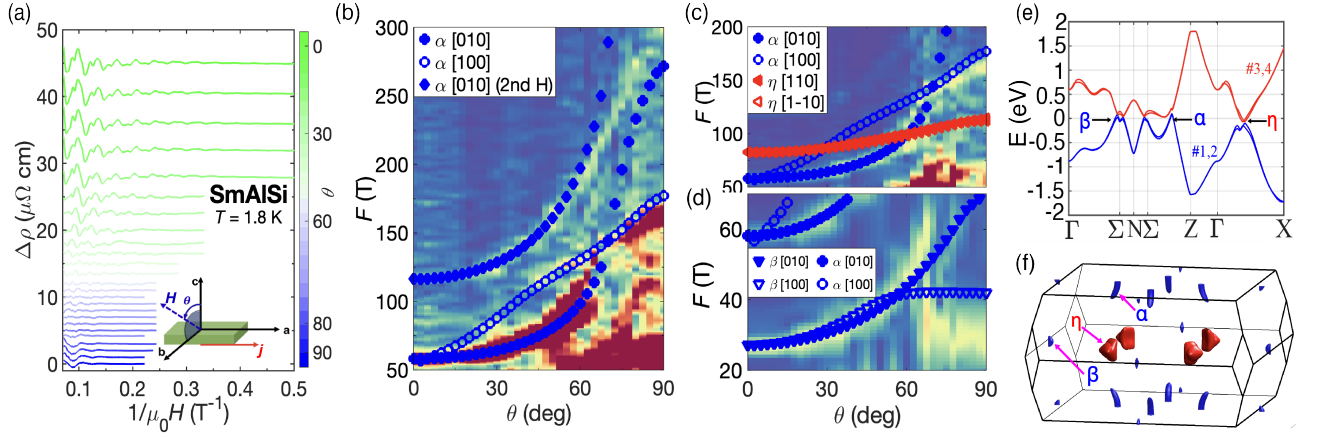


FIG. S7. Angle-dependent SdH oscillations of SmAlSi for $T = 1.8$ K (ordered state). (a) SdH oscillations from angle-dependent resistivity measurements after background subtraction. The measurement geometry is plotted in the inset. (b-d) Contour map of the FFT spectra in (a), with an emphasis on high frequency (b), medium frequency (c), and low frequency (d). The symbols represent calculated frequencies from cross-sections in DFT calculations. The [100] and [010] refers to the pockets that are located at k_x and k_y axis, respectively. (e) Partial band structure of SmAlSi in the PM state from DFT calculations [2]. Only the bands that cross the Fermi energy are shown here. (f) Partial Fermi surface from (e) showing the location of the Fermi pockets identified in Fig. S7(b-d).

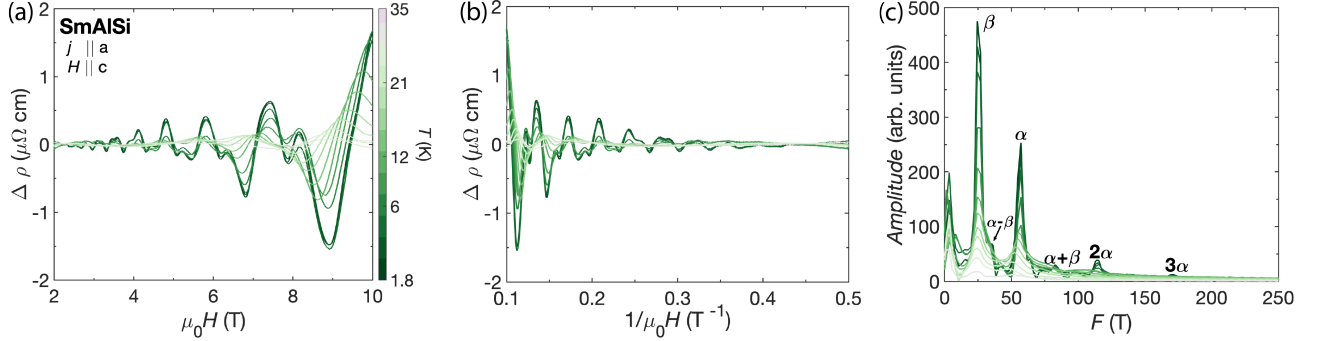


FIG. S8. Temperature-dependent SdH oscillations of SmAlSi. (a,b) Resistivity after background subtraction plotted as a function of the magnetic field $\mu_0 H$ (a) and a function of $1/\mu_0 H$ (b). (c) FFT spectra of the results in (b).

phases at different temperatures in NdAlSi.

Moreover, Wang et al [5] discovered QOs as a function of temperature at a constant magnetic field in the PM state, where the exchange interaction between the conduction electrons and 4f electrons appeared to be crucial. They propose that these signatures are due to the destructive interference between two QOs originating from the FS splitting, accompanied by a strong temperature- and magnetic field-dependent phase inversion.

Such QOs as a function of temperature are not discovered in SmAlSi. The exchange interaction between the conduction electrons and 4f electrons is expected to be significantly smaller in SmAlSi, given the small size of the Sm^{3+} effective moment ($\mu_{eff} = 0.714 \mu_B$) and polarized moment under field ($M = 0.05 \mu_B/Sm^{3+}$ at $T = 1.8$ K and $\mu_0 H = 9$ T). Therefore, the Fermi surface splitting in SmAlSi is dramatically suppressed.

We want to point out another possible reason for the quantum oscillation frequency shift. As shown in [6], the thermal broadening of the Fermi energy due to finite temperature will induce a frequency decrease with increasing temperature. Such an effect depends on the effective mass of the quasiparticles and is enhanced if the band dispersion is linear. The derivation in [6] is carried out in magnetic ions, which may further enhance the effect. This may explain the frequency shift of the frequency α .

The physics behind the QO frequency shift requires further investigation. This is outside the focus of this work and we will leave it to future studies.

The angle-dependent measurements are obtained at 1.8 K in the ordered state. We also performed the same measurements at 12 K in the PM state for completeness and to compare with results in [2]. The resulting SdH oscillations at various angles θ with $0 \leq \theta \leq 90^\circ$ are shown in Fig. S7(a). Similar to the QOs at 12 K, QOs are

observed in the entire range of θ . For $T = 1.8$ K, QOs onset can be observed starting at relatively low fields (~ 3 T), indicative of high crystal quality.

To build a correspondence between QOs and the FS, a comparison between experiments and calculation is required. The electronic structure of a magnetic material is correlated with the magnetic order. However, the large neutron absorption cross-section of the Sm atoms and the incommensurate structure make it difficult to resolve the magnetic structure from neutron scattering. Our isothermal magnetization measurements $M(H)$ [shown in Fig. S3(c)] indicate that the net magnetization is smaller than $0.05 \mu_B/\text{Sm}^{3+}$ up to the highest measured field of 9 T. Therefore, the magnetic order under field remains dominantly AFM and possibly retains the incommensurate nature. Given the uncertainty in determining the magnetic structure and the limitations of band structure calculations with incommensurate magnetic configuration, we compare the experimental QO results with the DFT prediction in the PM state. That is validated by: (1) the fact that the QO frequency is unchanged across the transition temperature and (2) the small moment of Sm^{3+} ($\mu_{sat}^{\text{Sm}^{3+}} = 0.714 \mu_B$) [3]. In a recent ARPES study by Lou *et al.* [7], no evident evolution of the band structure across the magnetic transitions.

Therefore, we used our calculations (reported in [2]) to match the experimental QO frequencies. The energy bands that cross the Fermi energy are shown in Fig. S7(e). At a first glance, four bands appear to cross the Fermi energy, forming multiple Fermi pockets [2]. However, the four bands that form these pockets are singly-degenerate, where the degeneracy is lifted by SOC and broken inversion symmetry I . We argue that consideration of only the spin-majority band is adequate here, for the following two reasons: the energy dispersion of the spin-majority/minority bands and the shape of the Fermi pockets from these bands is similar; under an external magnetic field, the conduction electrons are partially polarized along the field orientation, and the QOs of the corresponding bands are expected to dominate. Upon careful mapping between the extremal cross sections in theory and QO frequencies in experiments, we can identify the underlying Fermi pockets that contribute to the QOs, as shown in Fig. S7(b-d). The contour map of the QO frequencies at 1.8 K is similar to that at 12 K. The contour map of the QO frequencies consists of the following contributions: fundamental oscillations of pocket α (blue circles), the second harmonic of pocket α (blue diamonds), fundamental oscillations of pocket β (blue triangles), and fundamental oscillations of pocket η (red triangles). These Fermi pockets are plotted in Fig. S7(f). Compared to our previous results at 12 K [2], in addition to pocket α and pocket β , we found frequencies corresponding to pocket η and second harmonic of pocket α . The similarity of the contour maps between 1.8 K and 12 K also implies that it is unlikely to undergo a Fermi surface reconstruction in SmAlSi. These Fermi pockets are relevant to the Weyl points W1 and W2 that are close to the Fermi energy [2].

-
- [1] Yao, X., et al., Topological spiral magnetism in the Weyl semimetal SmAlSi. *Phys. Rev. X* **13**, 011035 (2023).
 - [2] Zhang, Y., et al., Kramers Nodal Lines and Weyl Fermions in SmAlSi. *Commun. Phys.* **6**, 134 (2023).
 - [3] Cao, W., et al., Quantum oscillations in noncentrosymmetric Weyl semimetal SmAlSi. *Chin. Phys. Lett* **39**, 047501 (2022).
 - [4] Gaudet, J., et al., Weyl-mediated helical magnetism in NdAlSi. *Nat. Mater.* **20**, 1650-1656 (2021).
 - [5] Wang, J., et al., Quantum oscillations in the magnetic Weyl semimetal NdAlSi arising from strong Weyl fermion–4f electron exchange interaction. *Phys. Rev. B* **108**, 024423 (2023).
 - [6] Guo, C., et al., Temperature dependence of quantum oscillations from non-parabolic dispersions . *Nat. Commun.* **12**, 6213 (2021).
 - [7] Lou, R., et al., Signature of weakly coupled f electrons and conduction electrons in magnetic Weyl semimetal candidates PrAlSi and SmAlSi. *Phys. Rev. B* **107**, 035158 (2023).